

---

# HiSin: Efficient High-Resolution Sinogram Inpainting via Resolution-Guided Progressive Inference

---

**Jiaze E**

Department of Computer Science  
William & Mary  
Williamsburg, VA 23185  
je@wm.edu

**Srutarshi Banerjee**

Data Science and Learning Division  
Argonne National Laboratory  
Lemont, IL 60439  
sruban@anl.gov

**Tekin Bicer**

Data Science and Learning Division  
Argonne National Laboratory  
Lemont, IL 60439  
tbicer@anl.gov

**Guannan Wang**

Department of Mathematics  
William & Mary  
Williamsburg, VA 23185  
gwang01@wm.edu

**Yanfu Zhang**

Department of Computer Science  
William & Mary  
Williamsburg, VA 23185  
yzhang105@wm.edu

**Bin Ren**

Department of Computer Science  
William & Mary  
Williamsburg, VA 23185  
bren@wm.edu

## Abstract

High-resolution sinogram inpainting is essential for computed tomography reconstruction, as missing high-frequency projections can lead to visible artifacts and diagnostic errors. Diffusion models are well-suited for this task due to their robustness and detail-preserving capabilities, but their application to high-resolution inputs is limited by excessive memory and computational demands. To address this limitation, we propose HiSin, a novel diffusion based framework for efficient sinogram inpainting via resolution-guided progressive inference. It progressively extracts global structure at low resolution and defers high-resolution inference to small patches, enabling memory-efficient inpainting. It further incorporates frequency-aware patch skipping and structure-adaptive step allocation to reduce redundant computation. Experimental results show that HiSin reduces peak memory usage by up to 31.25% and inference time by up to 18.15%, and maintains inpainting accuracy across datasets, resolutions, and mask conditions.

## 1 Introduction

A sinogram is a 2D projection-domain representation of computed tomography (CT) data, where each row corresponds to a different acquisition angle and each column to a detector position. However, in both industrial and medical settings, acquiring full sinograms is often impractical due to radiation exposure risks or scanning time constraints. Thus, sinogram inpainting plays a vital role in CT reconstruction, enabling recovery of projection data lost due to sensor malfunction, limited-angle acquisition, or radiation dose reduction [1].

High-resolution sinograms—such as  $2048 \times 2048$  or larger dimensions—are increasingly common with tomography experiments at synchrotron radiation facilities and in modern CT systems, e.g.,

in industrial inspection and medical diagnostics. In synchrotron radiation facilities, high spatial resolutions are critical to understand rapidly evolving phenomena such as crack propagation in materials, instabilities in batteries during cycling, and brain imaging [2, 3, 4, 5]. Such resolution demands also arise in clinical imaging, where accurately resolving tumor boundaries, tissue layering, or microlesions is essential for reliable diagnosis. Reducing resolution in such settings may cause diagnostic inaccuracies or delayed interventions, directly affecting patient health outcomes [6].

Diffusion models have demonstrated strong performance in image inpainting tasks due to their generative flexibility and ability to synthesize fine-grained structure [7, 8, 7, 9, 10]. However, when scaled to high-resolution inputs, their iterative denoising over full-resolution latent spaces leads to high memory and computational overheads. In real-world CT pipelines, inference is typically performed on one image at a time rather than in large batches. However, even in this single-image setting, the memory footprint of diffusion models can still exceed the capacity of common hardware.

These constraints are further exacerbated by practical deployment limitations. In industrial scenarios, CT systems are often embedded within compact workstations or inline inspection units, where hardware upgrades are restricted by power, space, and cooling constraints. Medical systems face similar challenges: large hospitals may have high-end GPUs, but those resources are heavily shared across multiple imaging pipelines and analysis workloads. Meanwhile, the majority of healthcare infrastructure worldwide—such as local clinics or mobile diagnostic units—operate under tight hardware budgets, where high-resolution diffusion model is infeasible. Cloud-based inference does not eliminate these barriers: compute quotas, multi-tenant scheduling, and shared memory pools prevent long-running diffusion tasks from monopolizing GPU memory. Furthermore, GPU schedulers typically reserve peak memory usage at job submission, rather than dynamically scaling during execution—making memory efficiency a hard constraint in practice.

A number of methods have been proposed to improve diffusion inference. Step distillation techniques [11, 12] reduce the number of denoising steps required for generation. Architecture-focused approaches [13, 14, 15] compress the model via architectural modifications or pruning. Trajectory-level optimization methods [16] focus on optimizing the sampling trajectory itself. While effective in RGB image domains, these methods do not address the structural challenges of sinogram data. They typically assume semantic continuity, uniform texture complexity, or fixed inference depth—assumptions that do not hold in the projection domain.

Sinograms are physical measurements governed by acquisition geometry. They contain highly directional structures, large smooth background regions, and frequency sparsity concentrated along specific angular bands. Crucially, sinogram patches remain physically meaningful when isolated—they correspond to narrower angular coverage or limited detector ranges, but still represent valid projections [17]. In contrast, natural image patches may lose semantic context (e.g., cropping only an eye from a face image), making patch-wise inference less suitable [18].

These domain differences motivate a rethinking of how diffusion inference should operate on sinograms. To this end, we propose HiSin, a high-resolution sinogram inpainting framework built around three design principles: hierarchical structure modeling, frequency-aware computation allocation, and structure-adaptive inference depth. First, we introduce a resolution-guided progressive inference scheme. Instead of processing the full-resolution image from the start, we perform denoising across a resolution hierarchy—beginning with a low-resolution version of the sinogram to extract global structure. This global prior is then used to guide patch-wise inference at higher resolutions. According to this progressive inference, we avoid full-frame activation and significantly reduce peak memory usage. Besides, unlike prior methods that rely on global embeddings, condition tokens, or architectural changes to maintain global context [19, 18, 20, 21], our approach maintains compatibility with pretrained models and operates entirely at inference time.

Second, in sinogram data, large background regions are structurally simple and spectrally sparse [17]. To avoid redundant computation in these areas, we introduce a frequency-aware patch-skipping mechanism that filters out low-energy patches using a simple FFT-based score. These patches are bypassed during inference and approximated using latent-level representations, reducing computation without affecting inpainting fidelity.

Third, for patches that are retained, local complexity varies significantly—from flat gradients to fine structural edges. To better align inference cost with content richness, we apply a structure-adaptive denoising scheduler. Each patch is assigned a custom number of denoising steps based on a

complexity score that combines Shannon entropy [22] and frequency energy, allowing the model to allocate computation where detail is present and skip over simple regions.

Together, these designs preserve inpainting fidelity by first capturing global structure that maintains long-range consistency across resolution levels. Patch skipping removes only regions with negligible signal, ensuring that no structurally relevant information is lost, while adaptive denoising assigns each patch a sufficient number of steps based on its complexity, preventing under-computation in detail-rich areas. As a result, HiSin improves efficiency (both in peak memory usage and inference speed) without compromising inpainting quality. In summary, our contributions are as follows:

- We propose HiSin, a resolution-guided diffusion framework that restructures the inference process to support high-resolution sinogram inpainting under strict memory constraints. It uses resolution as an inference scheduling dimension—progressively extracting global structure at low resolution to guide spatially segmented computation at high resolution. It avoids full-frame activation, maintains long-range consistency, and operates entirely at inference time *without retraining or architectural modifications*.
- We introduce two novel inference time mechanisms—frequency-aware patch skipping and structure-adaptive step allocation—designed specifically to exploit the directional structure and spectral sparsity of sinogram data. These components reduce inference cost by eliminating redundant computation in low-information regions and adapting denoising effort based on local signal complexity. Both mechanisms are derived from statistical properties unique to projection-domain measurements.
- HiSin successfully enables  $2048 \times 2048$  sinogram inpainting on an A100 GPU, reducing peak memory by up to 31.25% and inference time by up to 18.15% without compromising inpainting quality across multiple datasets, input resolutions, and mask ratios.

## 2 Related Work

**Inpainting Methods for RGB and Projection-domain Images.** Diffusion-based models have achieved strong performance on image inpainting due to their generative capacity and ability to model uncertainty. Methods such as RePaint [9], Palette [10], Blended Diffusion [19], and CoPaint [18] enhance global coherence on RGB images through iterative sampling or semantic priors. However, these methods assume spatially dense textures and uniform semantics, which do not align with the structural properties of projection-domain data such as sinograms. Sinogram inpainting has also been studied in industrial and medical CT settings using CNNs, GANs, transformer-based and diffusion-based models for sparse-view recovery or artifact reduction [23, 24], but these works generally ignore memory constraints and inference time optimizations.

**Inference Acceleration in Diffusion Models.** Improving the efficiency of diffusion inference has become a growing area of focus. Sampling-based methods reduce denoising steps through distillation [11], or step-aware training [25]. Architectural methods operate in latent space or employ memory-aware attention, such as in HiDiffusion [26] and DiffIR [27]. Model pruning and lightweight design strategies have also been proposed, as seen in SnapFusion [13], Effortless Efficiency [14], and DiP-GO [15]. Patch-wise generation and conditional masking [28] have also been explored to control computation scope. However, most existing methods require retraining, loss rebalancing, or internal modifications to the model. Many of these approaches are orthogonal to our work and can be integrated in principle, but they do not account for the structural characteristics of sinogram data, such as directional sparsity and local interpretability. Applying them effectively in this domain would require additional adaptation.

**Memory and Runtime Efficient Deep Learning.** Beyond diffusion, memory- and latency-aware inference strategies have been widely studied in deep learning. Techniques include recomputation and memory reuse [29, 30], and runtime-adaptive depth scaling [31]. MEST [32] also explore sparsity-aware training or deployment under tight memory budgets. These techniques address memory bottlenecks in standard feedforward networks and our work focuses instead on iterative generative models with different constraints.

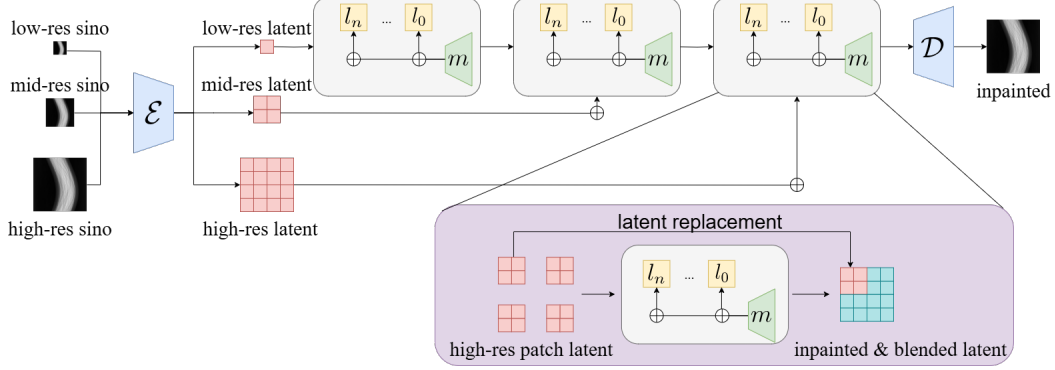


Figure 1: Overview of HiSin. The input sinogram is inpainted through a three-stage progressive inference pipeline: low, mid, and high-resolution stages. Each box labeled  $l_n$  and  $l_0$  represents a multi-step DDIM denoising process of the latent guided by mask  $m$ .  $\mathcal{E}$  and  $\mathcal{D}$  stand for encoder and decoder. The lower module depicts frequency-aware patch skipping and structure-adaptive denoising, which are applied during the high-resolution stage.

### 3 HiSin: High-Resolution Sinogram Inpainting

As shown in Figure 1, HiSin reconstructs missing sinogram data in three stages: a coarse low-resolution estimating global structure is then progressively refined at mid and high resolutions. This hierarchy reduces memory usage and preserves global consistency but introduces two challenges at full resolution: redundant computation in simple regions and suboptimal inference allocation. To address this, HiSin adds two lightweight modules: frequency-aware patch skipping to ignore low-information areas, and a structure-adaptive denoising scheduler that adjusts sampling steps based on local complexity.

#### 3.1 FCDM and Generality of the Inference Framework

HiSin is implemented on top of FCDM [33], a two-stage diffusion-based sinogram inpainting model. FCDM first encodes the input sinogram into a latent representation using an encoder-decoder backbone enhanced with bidirectional frequency-domain convolutions, capturing both spatial and spectral structures. In the second stage, diffusion is performed in the latent space, guided by Fourier-enhanced mask embeddings and frequency-adaptive noise scheduling, which aligns the denoising process with the inherent spectral dynamics of sinograms. FCDM further incorporates a physics-guided loss that softly enforces total absorption consistency, improving generalization under realistic scan variations.

We adopt FCDM primarily for its alignment with projection-domain data and its modular design. However, our proposed improvements—including resolution-guided inference, patch skipping, and adaptive step allocation—operate entirely at the inference level and do not depend on FCDM’s specific architectural components. These strategies can be applied to other diffusion-based sinogram inpainting models and operate independently of the model architecture and training objectives.

#### 3.2 Resolution-Guided Progressive Inference

To efficiently inpaint high-resolution sinograms while avoiding memory overflow, HiSin adopts a three-stage progressive inference pipeline operating over low, mid, and high resolutions. Let  $x_r$  denote the input at resolution  $r \in \{low, mid, high\}$ . Each resolution level  $x_r$  is obtained by downsampling the original sinogram using a fixed ratio: low and mid-resolution inputs correspond to  $0.25\times$  and  $0.5\times$  the original resolution, respectively. All three versions are then encoded independently by a shared encoder  $\mathcal{E}(\cdot)$ , ensuring that each latent  $z_r = \mathcal{E}(x_r)$  preserves resolution-aligned structural semantics. At the first stage, full DDIM inference is performed on  $z_{low}$  to generate a coarse prior  $\hat{z}_{low}$ , which captures global structural cues at minimal memory cost.

In the second stage, we refine the geometry at mid-resolution. The latent  $z_{mid}$  is fused with the upsampled output from the previous stage using a resolution-aware weighted sum:

$$\tilde{z}_{mid} = \lambda_{mid} \cdot Up(\hat{z}_{low}) + (1 - \lambda_{mid}) \cdot z_{mid},$$

where  $\lambda_{low} \in [0, 1]$  is a scalar controlling the fusion strength, and  $Up(\cdot)$  denotes nearest-neighbor upsampling. This fusion helps the model retain mid-level structure while reinforcing global context. The resulting  $\tilde{z}_{mid}$  is then denoised via DDIM to produce  $\hat{z}_{mid}$ .

At the final stage, we operate on the original full-resolution input. After the high resolution sinogram  $x_{high}$  being encoded into latent  $z_{high}$ , we divide  $z_{high}$  into non-overlapping patches  $\{z_{high}^i\}$ . Each patch is of fixed size, ensuring consistent inference cost per patch across resolutions. For each patch, we retrieve the aligned region from  $\hat{z}_{mid}$ , upsample it, and fuse it with the local patch latent:

$$\tilde{z}_{high}^i = \lambda_{high} \cdot Up(\hat{z}_{mid}^i) + (1 - \lambda_{high}) \cdot z_{high}^i.$$

Each  $\tilde{z}_{high}^i$  is then denoised via DDIM. Sec 3.3 and Sec 3.4 introduce more details about the final stage. This patch-wise processing avoids full-frame memory load while preserving long-range consistency through hierarchical conditioning. Each patch is processed sequentially during inference to ensure bounded memory usage.

### 3.3 Frequency-Aware Patch Skipping

High-resolution sinograms often contain broad low-frequency backgrounds with narrow high-frequency details. To reduce computation in low-complexity regions, HiSin introduces frequency-aware patch skipping based on localized spectral content.

#### 3.3.1 Frequency-Aware Patch Pruning

To reduce unnecessary computation in low-information regions of high-resolution sinograms, we introduce frequency-aware patch skipping. Let  $P$  denote a high-resolution image patch, and let  $\mathcal{F}(P)$  represent its real-valued 2D Fourier transform. We define the high-frequency energy ratio  $\gamma(P)$  as:

$$\gamma(P) = \frac{\sum_{(u,v) \in \Omega_{high}} |\mathcal{F}(P)_{u,v}|^2}{\sum_{(u,v)} |\mathcal{F}(P)_{u,v}|^2},$$

where  $\Omega_{high}$  is a predefined high-pass band, typically the outer third of the frequency spectrum. A low value of  $\gamma(P)$  indicates that the patch is dominated by low-frequency content, i.e., structurally smooth or empty regions. If  $\gamma(P) < \tau$ , the patch is deemed spectrally sparse.

Rather than running full DDIM inference for spectrally sparse patches, we replace their latent outputs with a fixed approximation. This latent is obtained by passing a synthetic input patch—filled with low-amplitude Gaussian noise with mean 0, and standard deviation 0.01—through the original FCDM encoder and DDIM steps. This design simulates typical background regions. It avoids repeated computation in trivial regions and ensures consistency with standard outputs.

#### 3.3.2 Cosine-Based Patch Blending

To avoid visual artifacts at patch boundaries, particularly when adjacent regions are inferred with different mechanisms, we apply a smooth blending operation between neighboring patches. This is especially important in high-resolution sinograms where directional continuity must be preserved.

Let  $P_1$  and  $P_2$  denote two horizontally adjacent reconstructed patches, and  $p \in [0, L]$  be local coordinate across boundary region of width  $L$  pixels. Define a cosine-based spatial weight function:

$$\alpha(p) = \frac{1}{2} \left( 1 - \cos\left(\frac{\pi p}{L}\right) \right),$$

which increases smoothly from 0 to 1 across the boundary. The blended pixel value is computed as:

$$P_{blend}(x, y) = \alpha(p) \cdot P_1(x, y) + (1 - \alpha(p)) \cdot P_2(x, y).$$

This produces a smooth interpolation where the transition is soft and visually imperceptible, reducing abrupt intensity jumps at patch edges.

We apply this blending only when necessary. Specifically, we compute the average gradient magnitude in the overlapping region using a standard Sobel filter applied to the corresponding mid-resolution sinogram. If the gradient exceeds a predefined threshold  $\eta$ , blending is enabled; otherwise, a simple hard stitch is used to save computation in flat areas. This conditional mechanism ensures efficiency without compromising visual consistency in structurally complex regions.

### 3.4 Structure-Adaptive Denoising

To further reduce computation, we allocate a different number of denoising steps to each patch based on its structural complexity. Unlike static diffusion sampling—where every region receives the same number of DDIM steps—we adapt the inference depth dynamically to match the content difficulty.

#### 3.4.1 Complexity Score Computation

Let  $P$  denote a patch in the high-resolution sinogram. We define a complexity score  $\kappa(P)$  that combines two frequency-domain measures: Shannon entropy and high-frequency energy. The Shannon entropy  $\mathcal{H}(P)$  is computed over the pixel intensity histogram:

$$\mathcal{H}(P_i) = - \sum_j p_j \log p_j,$$

where  $p_j$  is the normalized count of pixel intensity in bin  $i$ . This captures texture randomness and distribution uniformity.

Also, we compute the spectral energy using the L1-norm of the 2D FFT of the patch. The overall complexity score is defined as:

$$\kappa_i = \mathcal{H}(P_i) + \log(1 + \|\mathcal{F}(P_i)\|_1),$$

where  $\mathcal{F}(P_i)$  is the 2D real-valued FFT of the patch and  $\|\cdot\|_1$  denotes the L1-norm of the spectrum.

Entropy captures randomness and texture variation in the spatial domain, while the FFT energy captures signal richness and directional complexity. Their combination provides a robust, domain-agnostic proxy for structural difficulty.

#### 3.4.2 Patch-Wise Step Mapping

To convert  $\kappa_i$  into a patch-specific number of denoising steps, we apply a sigmoid-based scaling function:

$$S_i = \lfloor S_{min} + (S_{max} - S_{min}) \cdot \sigma(\beta(\kappa_i - \mu)) \rfloor$$

where  $\mu$  is the mean complexity across all patches in the sinogram;  $\beta$  controls the steepness of the sigmoid transition;  $\sigma(\cdot)$  is the standard sigmoid function;  $S_{min}, S_{max}$  define the step range;  $\lfloor \cdot \rfloor$  denotes rounding down to the nearest integer.

This formulation ensures a soft but data-driven allocation: patches with below-average complexity receive fewer sampling steps, while those above the mean are modeled more deeply. Using the sigmoid ensures that step variation remains smooth, differentiable, and robust to outliers. The centering around the mean further normalizes the step distribution across sinograms with varying overall complexity.

Each patch in the high-resolution stage follows its individually assigned DDIM schedule, allowing inference effort to be concentrated where structural ambiguity is high.

## 4 Evaluation

This section compares HiSin with three state-of-the-art baselines: FCDM [33], DiffIR [27], and HiDiffusion [26]. The evaluation has two main objectives: (1) demonstrating that HiSin significantly improves memory efficiency and inference speed while maintaining inpainting quality (Sec 4.2); (2) conducting ablation studies to validate the effectiveness of our mechanisms, including frequency-aware patch skipping and structure-adaptive denoising (Sec 4.3).

## 4.1 Experimental Setup

**Evaluation Platform and Settings.** All experiments use NVIDIA A100 GPUs with 40 GB on-device memory, CUDA 12.2, and PyTorch 2.1.0. Unless otherwise stated, all inference is performed on a single A100 card from the Polaris supercomputer of Argonne Leadership Computing Facility (ALCF) resources at Argonne National Laboratory (ANL)<sup>1</sup>. All implementations employ PyTorch built-in optimizations: `torch.compile()` to enable graph-mode execution, mixed-precision inference via `torch.autocast()` (fp16), and `torch.backends.cudnn.benchmark = True` for kernel tuning.

All diffusion-based experiments use the denoising diffusion implicit models (DDIM) [34] sampler with 50 steps. This step count is consistent with values evaluated in DDIM, where 50-step sampling achieves a strong balance between quality and efficiency. All inference is performed with a batch size of 1. Patch size is fixed to  $32 \times 32$ , following standard practice in vision transformer-based architectures such as MAE [35], where this granularity captures sufficient context while remaining memory-efficient. For patch skipping, the high-frequency threshold is set to  $\tau = 0.08$ , which empirically filters low-information patches without affecting inpainting fidelity. For adaptive step scheduling, we use  $(S_{min}, S_{max}) = (10, 50)$  to stay within the DDIM step budget while allowing fine-grained inference depth.

To ensure fair comparison, all baseline models are retrained from scratch using their official codebases. Since HiSin operates entirely at inference time, no retraining or task-specific fine-tuning is applied. Each dataset provides 100,000 training samples at  $512 \times 512$  resolution and 50 test samples. We evaluate all models at three resolutions— $2048 \times 2048$ ,  $1024 \times 1024$ , and  $512 \times 512$ —to assess scalability in memory, runtime, and accuracy. For memory and runtime evaluation, the mask ratio is fixed at 0.8. For accuracy evaluation, all models are tested under three mask ratios: 0.4, 0.6, and 0.8. Evaluation is conducted under identical conditions across methods.

**Dataset.** We evaluate three datasets Real-world, Shape, and Shepp2d, each tested at three resolutions:  $2048 \times 2048$ ,  $1024 \times 1024$ , and  $512 \times 512$ . Real-world dataset [36] consists of real sinogram images obtained from various materials and objects, derived from actual synchrotron radiation CT experiments, including Advanced Photon Source (APS)<sup>2</sup> at ANL. It also includes samples with dynamic features [37] and in situ [38] measurements, which capture a wide range of experiments at APS and other synchrotron facilities. This dataset reflects realistic acquisition noise, incomplete coverage, and other imperfections. Shape dataset generated using the scikit-image library [39] contains a variety of simulated geometric shapes, including circles, rectangles, and triangles. It is designed to introduce varied patterns and controlled shape-based structures. Shepp2d dataset generated by the Tomopy library [40] comprises simulated shepp-logan phantoms used in simulation-based CT research. It consists of stable, analytically defined sinograms widely serving as sinogram inpainting benchmarks.

**Metrics.** We evaluate each method using both efficiency and quality metrics. For computational performance, we report peak GPU memory usage and average inference runtime, measured over multiple forward passes on a single A100 GPU. Peak memory reflects the maximum GPU allocation during inference, indicating worst-case hardware demand. For inpainting fidelity, we use Structural Similarity Index (SSIM) [41] and Peak Signal-to-Noise Ratio (PSNR). SSIM captures perceptual and structural consistency, important for projection-domain data, while PSNR quantifies absolute pixel-wise differences, enabling comparison across varying noise and sparsity levels.

**Baselines.** We compare HiSin with three representative baselines: FCDM [33], HiDiffusion [26], and DiffIR [27]. FCDM is a recent diffusion-based sinogram inpainting model, and serves as the pretrained backbone for HiSin. HiDiffusion is designed for scalable high-resolution diffusion, improving memory efficiency through resolution-aware U-Net design and localized attention—without requiring retraining. It addresses the same high-resolution generation challenges as HiSin under similar inference-only constraints. DiffIR focuses on image restoration tasks, introducing a compact intermediate prior to reduce the effective number of sampling steps. It targets the same inpainting task category and shares the goal of reducing inference overhead.

---

<sup>1</sup>Polaris Cluster at ALCF: <https://www.alcf.anl.gov/polaris>

<sup>2</sup>Advanced Photon Source: <https://www.aps.anl.gov>

Table 1: Peak GPU memory usage (GB) and inference time (s) for different methods w/ varied input resolutions. 'OOM' indicates out-of-memory failure. All results are measured on a single A100 GPU. *Results are averaged across three datasets.*

| Method       | 2048×2048   |             | 1024×1024  |             | 512×512    |             |
|--------------|-------------|-------------|------------|-------------|------------|-------------|
|              | Peak GPU    | Inf time    | Peak GPU   | Inf time    | Peak GPU   | Inf time    |
| FCDM         | OOM         |             | 16.2       | 1.21        | 5.2        | 0.6         |
| DiffIR       | OOM         |             | 14.6       | 0.98        | 4.8        | 0.49        |
| HiDiffusion  | 35.7        | 2.7         | 12.5       | 0.92        | 4.1        | 0.46        |
| HiSin (ours) | <b>24.9</b> | <b>2.21</b> | <b>8.7</b> | <b>0.78</b> | <b>3.3</b> | <b>0.40</b> |

## 4.2 Overall Quantitative and Qualitative Results

This section presents both quantitative and qualitative comparisons. Due to space constraints, quantitative results are resolution-based *averages* over three datasets. Per-dataset details are in Appendix.

**Peak Memory Usage Comparison.** We begin with evaluating the memory efficiency of HiSin. As shown in Table 1, using all three datasets for each resolution, with a fixed mask ratio of 0.8, our method significantly reduces peak GPU memory usage compared to prior methods across all tested resolutions. The original unoptimized model FCDM [33] and DiffIR [27] both encounter out-of-memory (OOM) failures at  $2048 \times 2048$  resolution, indicating that standard diffusion pipelines cannot scale to such resolutions even with a high-end GPU. In contrast, HiSin remains fully operational under these conditions. Overall, HiSin achieves up to a 30.25% reduction in memory usage relative to the most efficient baseline HiDiffusion. Notably, this trend holds consistently across input sizes, indicating that our framework scales gracefully.

**Inference Time Comparison.** Table 1 reports inference times using all three datasets for each resolution, with a fixed mask ratio of 0.8. HiSin consistently achieves faster inference than the fastest baseline, HiDiffusion, with speedup up to 18.5% across all tested input sizes. These improvements stem from two sources: progressive scheduling reduces redundant steps in simple regions, while patch skipping eliminates computation entirely for spectrally sparse areas. Together, they allow HiSin to allocate effort where needed while avoiding over-computation elsewhere. This demonstrates that high-resolution efficiency can be achieved without sacrificing execution time.

**Inpainting Quality.** Table 2 summarizes accuracy results. HiSin preserves output quality while reducing memory and computation, achieving SSIM and PSNR scores nearly identical to the original model (FCDM) across various mask ratios—shown for sinograms (outside parentheses) and reconstructions (inside). Compared to DiffIR and HiDiffusion, HiSin achieves higher inpainting accuracy in both metrics. Figure 2 visualizes inpainting sinogram images and reconstructed images on Real-world dataset, Shape dataset, and Shepp2d dataset with 0.8 mask ratio. HiSin and the original model FCDM produce nearly indistinguishable outputs. This further supports our conclusion that HiSin maintains high visual fidelity while significantly improving efficiency.

## 4.3 Ablation Studies

To analyze the impact of individual components in HiSin, we perform ablation studies targeting the two core mechanisms: adaptive denoising based on structural complexity, and sparse patch skipping based on spectral sparsity. Table 3 summarizes the results across three resolutions. Removing the adaptive denoising module and assigning the same number of sampling steps to all patches leads to increased inference time—an average increase of 26.84% without adaptive steps (all set as 50) and an average increase of 32.13% without patch skipping—while memory usage remains unchanged. Notably, SSIM and PSNR are nearly identical, confirming that the adaptive schedule preserves quality while avoiding redundant computation. These results confirm that the two mechanisms are complementary: adaptive denoising reduces computational depth, while patch skipping reduces spatial workload. Together, they form an effective strategy for efficient high-resolution inpainting.

Table 2: Quantitative SSIM and PSNR comparisons across all datasets, resolutions, and mask ratios. For each method, SSIM is shown on the first line, PSNR on the second, *averaged over three datasets*. Each entry is formatted as: inpainted sinogram (CT reconstruction), with metrics computed only within masked regions.

|           | Methods      | Mask ratio                                 |   |  |
|-----------|--------------|--|---|--|
|           |              | 0.4  | 0.6   | 0.8  |
| 2048×2048 | HiSin (ours) | <b>0.921 (0.908)</b><br><b>30.5 (29.7)</b> | <b>0.930 (0.916)</b><br><b>30.9 (29.9)</b>  | <b>0.934 (0.920)</b><br><b>30.8 (29.8)</b> |
|           | FCDM         | OOM<br>OOM                                 | OOM<br>OOM                                  | OOM<br>OOM                                 |
|           | HiDiffusion  | 0.898 (0.865)<br>28.8 (28.0)               | 0.903 (0.899)<br>29.1 (28.7)                | 0.907 (0.885)<br>29.0 (28.8)               |
|           | DiffIR       | OOM<br>OOM                                 | OOM<br>OOM                                  | OOM<br>OOM                                 |
|           |              |  |   |  |
| 1024×1024 | HiSin (ours) | <b>0.927 (0.914)</b><br><b>31.3 (30.4)</b> | <b>0.934 (0.920)</b><br><b>31.4 (30.4)</b>  | <b>0.938 (0.925)</b><br><b>31.4 (30.6)</b> |
|           | FCDM         | <b>0.927 (0.915)</b><br><b>31.3 (30.4)</b> | <b>0.935 (0.922 )</b><br><b>31.5 (30.6)</b> | <b>0.940 (0.926)</b><br><b>31.6 (30.7)</b> |
|           | HiDiffusion  | 0.895 (0.880)<br>29.9 (28.8)               | 0.904 (0.889)<br>29.7 (29.0)                | 0.906 (0.895)<br>29.9 (28.2)               |
|           | DiffIR       | 0.889 (0.878)<br>29.4 (28.6)               | 0.892 (0.880)<br>29.4 (28.2)                | 0.894 (0.883)<br>29.7 (28.6)               |
|           |              |  |   |  |
| 512×512   | HiSin (ours) | <b>0.923 (0.910)</b><br><b>31.1 (30.3)</b> | <b>0.929 (0.916)</b><br><b>31.4 (30.6)</b>  | <b>0.934 (0.922)</b><br><b>31.6 (30.8)</b> |
|           | FCDM         | <b>0.925 (0.912)</b><br><b>31.2 (30.4)</b> | <b>0.930 (0.917)</b><br><b>31.5 (30.7)</b>  | <b>0.936 (0.924)</b><br><b>31.7 (30.9)</b> |
|           | HiDiffusion  | 0.895 (0.881)<br>29.6 (28.9)               | 0.899 (0.883)<br>29.9 (29.0)                | 0.910 (0.887)<br>30.1 (29.1)               |
|           | DiffIR       | 0.894 (0.883)<br>29.3 (28.5)               | 0.906 (0.891)<br>29.3 (28.6)                | 0.909 (0.889)<br>30.0 (28.0)               |
|           |              |  |   |  |

Table 3: Ablation study of adaptive denoising and patch skipping in HiSin. Metrics include inference time (s), peak memory (GB), and SSIM/PSNR with 0.8 mask ratio, *averaged over three datasets*.

|           | Method             | Inf time | Peak mem | SSIM  | PSNR |
|-----------|--------------------|----------|----------|-------|------|
| 2048×2048 | HiSin              | 2.21     | 24.9     | 0.934 | 30.8 |
|           | W/o adaptive steps | 3.05     | 24.9     | 0.935 | 30.9 |
|           | W/o patch skipping | 3.25     | 24.9     | 0.936 | 30.9 |
| 1024×1024 | HiSin              | 0.78     | 8.7      | 0.938 | 31.4 |
|           | W/o adaptive steps | 1.05     | 8.7      | 0.939 | 31.5 |
|           | W/o patch skipping | 1.15     | 8.7      | 0.939 | 31.5 |
| 512×512   | HiSin              | 0.40     | 3.3      | 0.934 | 31.6 |
|           | W/o adaptive steps | 0.55     | 3.3      | 0.935 | 31.6 |
|           | W/o patch skipping | 0.59     | 3.3      | 0.935 | 31.6 |

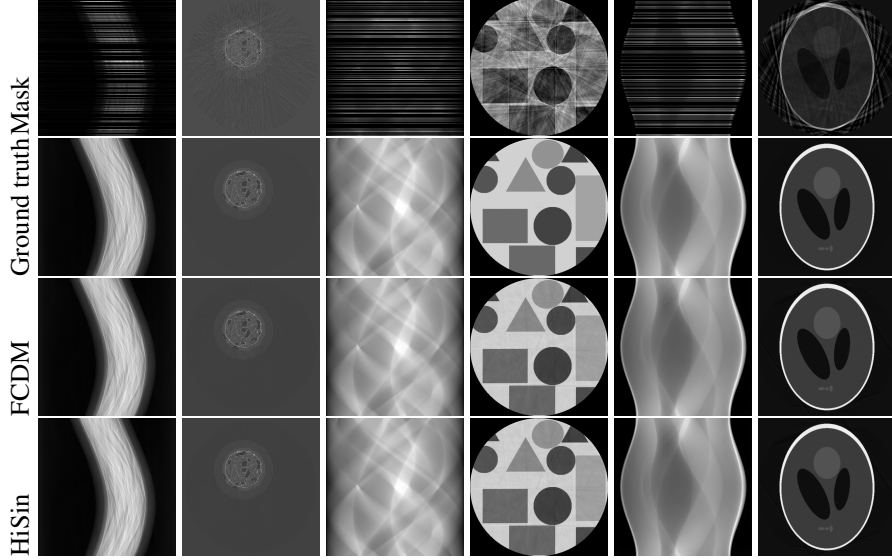


Figure 2: Qualitative inpainting results on the Real-world dataset (column 1 to 2), Shape dataset (column 3 to 4), and Shepp2d dataset (column 5 to 6) with 0.8 mask ratio at  $1024 \times 1024$  resolution. Odd columns and even columns show the sinogram and reconstructed images, respectively.

## 5 Conclusion & Limitations

We present HiSin, a novel framework for efficient high-resolution sinogram inpainting. To address the GPU memory limitations that hinder diffusion-based models at large input scales, HiSin integrates mechanisms that adaptively allocate computation across resolutions, spatial regions, and inference depth. This design enables inpainting on  $2048 \times 2048$  sinograms using a single GPU, significantly reducing memory usage and runtime while maintaining the inpainting fidelity. However, HiSin may slightly increase the total computation load in terms of FLOPs; more details are discussed in the Appendix.

## References

- [1] Willi A Kalender. *Computed tomography: fundamentals, system technology, image quality, applications*. John Wiley & Sons, 2011.
- [2] Chen Zhao, Chuanwei Wang, Xiang Liu, Inhui Hwang, Tianyi Li, Xinwei Zhou, Jiecheng Diao, Junjing Deng, Yan Qin, Zhenzhen Yang, et al. Suppressing strain propagation in ultrahigh-ni cathodes during fast charging via epitaxial entropy-assisted coating. *Nature Energy*, 9(3):345–356, 2024.
- [3] Viktor Nikitin, Vincent De Andrade, Azat Slyamov, Benjamin J Gould, Yuepeng Zhang, Vandana Sampathkumar, Narayanan Kasthuri, Doğa Gürsoy, and Francesco De Carlo. Distributed optimization for nonrigid nano-tomography. *IEEE Transactions on Computational Imaging*, 7:272–287, 2021.
- [4] Eva L Dyer, William Gray Roncal, Judy A Prasad, Hugo L Fernandes, Doga Gürsoy, Vincent De Andrade, Kamel Fezzaa, Xianghui Xiao, Joshua T Vogelstein, Chris Jacobsen, et al. Quantifying mesoscale neuroanatomy using x-ray microtomography. *eneuro*, 4(5), 2017.
- [5] Mert Hidayetoğlu, Tekin Bicer, Simon Garcia De Gonzalo, Bin Ren, Vincent De Andrade, Doga Gursoy, Raj Kettimuthu, Ian T Foster, and Wen-mei W Hwu. Petascale xct: 3d image reconstruction with hierarchical communications on multi-gpu nodes. In *SC20: International Conference for High Performance Computing, Networking, Storage and Analysis*, pages 1–13. IEEE, 2020.
- [6] Maciej A Mazurowski. Radiogenomics: what it is and why it is important. *Journal of the American College of Radiology*, 12(8):862–866, 2015.
- [7] Jonathan Ho, Ajay Jain, and Pieter Abbeel. Denoising diffusion probabilistic models. *Advances in neural information processing systems*, 33:6840–6851, 2020.
- [8] Jascha Sohl-Dickstein, Eric Weiss, Niru Maheswaranathan, and Surya Ganguli. Deep unsupervised learning using nonequilibrium thermodynamics. In *International conference on machine learning*, pages 2256–2265. pmlr, 2015.
- [9] Andreas Lugmayr, Martin Danelljan, Andres Romero, Fisher Yu, Radu Timofte, and Luc Van Gool. Repaint: Inpainting using denoising diffusion probabilistic models. In *Proceedings of the IEEE/CVF conference on computer vision and pattern recognition*, pages 11461–11471, 2022.
- [10] Chitwan Saharia, William Chan, Huiwen Chang, Chris Lee, Jonathan Ho, Tim Salimans, David Fleet, and Mohammad Norouzi. Palette: Image-to-image diffusion models. In *ACM SIGGRAPH 2022 conference proceedings*, pages 1–10, 2022.
- [11] Tim Salimans and Jonathan Ho. Progressive distillation for fast sampling of diffusion models. *arXiv preprint arXiv:2202.00512*, 2022.
- [12] Chenlin Meng, Robin Rombach, Ruiqi Gao, Diederik Kingma, Stefano Ermon, Jonathan Ho, and Tim Salimans. On distillation of guided diffusion models. In *Proceedings of the IEEE/CVF Conference on Computer Vision and Pattern Recognition*, pages 14297–14306, 2023.
- [13] Yanyu Li, Huan Wang, Qing Jin, Ju Hu, Pavlo Chemerys, Yun Fu, Yanzhi Wang, Sergey Tulyakov, and Jian Ren. Snapfusion: Text-to-image diffusion model on mobile devices within two seconds. *Advances in Neural Information Processing Systems*, 36:20662–20678, 2023.
- [14] Yang Zhang, Er Jin, Yanfei Dong, Ashkan Khakzar, Philip Torr, Johannes Stegmaier, and Kenji Kawaguchi. Effortless efficiency: Low-cost pruning of diffusion models. *arXiv preprint arXiv:2412.02852*, 2024.
- [15] Haowei Zhu, Dehua Tang, Ji Liu, Mingjie Lu, Jintu Zheng, Jinzhang Peng, Dong Li, Yu Wang, Fan Jiang, Lu Tian, et al. Dip-go: A diffusion pruner via few-step gradient optimization. *Advances in Neural Information Processing Systems*, 37:92581–92604, 2024.
- [16] Cheng Lu, Yuhao Zhou, Fan Bao, Jianfei Chen, Chongxuan Li, and Jun Zhu. Dpm-solver: A fast ode solver for diffusion probabilistic model sampling in around 10 steps. *Advances in Neural Information Processing Systems*, 35:5775–5787, 2022.
- [17] Malcolm Slaney and AC Kak. *Principles of computerized tomographic imaging*. IEEE press, 1988.
- [18] Guanhua Zhang, Jiabao Ji, Yang Zhang, Mo Yu, Tommi S Jaakkola, and Shiyu Chang. Towards coherent image inpainting using denoising diffusion implicit models. 2023.
- [19] Omri Avrahami, Dani Lischinski, and Ohad Fried. Blended diffusion for text-driven editing of natural images. In *Proceedings of the IEEE/CVF conference on computer vision and pattern recognition*, pages 18208–18218, 2022.

- [20] Narek Tumanyan, Michal Geyer, Shai Bagon, and Tali Dekel. Plug-and-play diffusion features for text-driven image-to-image translation. In *Proceedings of the IEEE/CVF Conference on Computer Vision and Pattern Recognition*, pages 1921–1930, 2023.
- [21] Lvmin Zhang, Anyi Rao, and Maneesh Agrawala. Adding conditional control to text-to-image diffusion models. In *Proceedings of the IEEE/CVF international conference on computer vision*, pages 3836–3847, 2023.
- [22] Claude E Shannon. A mathematical theory of communication. *The Bell system technical journal*, 27(3):379–423, 1948.
- [23] Hoyeon Lee, Jongha Lee, Hyeongseok Kim, Byungchul Cho, and Seungryong Cho. Deep-neural-network-based sinogram synthesis for sparse-view ct image reconstruction. *IEEE Transactions on Radiation and Plasma Medical Sciences*, 3(2):109–119, 2018.
- [24] Kyong Hwan Jin, Michael T McCann, Emmanuel Froustey, and Michael Unser. Deep convolutional neural network for inverse problems in imaging. *IEEE transactions on image processing*, 26(9):4509–4522, 2017.
- [25] Guangxuan Xiao, Tianwei Yin, William T Freeman, Frédo Durand, and Song Han. Fastcomposer: Tuning-free multi-subject image generation with localized attention. *International Journal of Computer Vision*, pages 1–20, 2024.
- [26] Shen Zhang, Zhaowei Chen, Zhenyu Zhao, Yuhao Chen, Yao Tang, and Jiajun Liang. Hidiffusion: Unlocking higher-resolution creativity and efficiency in pretrained diffusion models. In *European Conference on Computer Vision*, pages 145–161. Springer, 2024.
- [27] Bin Xia, Yulun Zhang, Shiyin Wang, Yitong Wang, Xinglong Wu, Yapeng Tian, Wenming Yang, and Luc Van Gool. Diffir: Efficient diffusion model for image restoration. In *Proceedings of the IEEE/CVF International Conference on Computer Vision*, pages 13095–13105, 2023.
- [28] Omri Avrahami, Ohad Fried, and Dani Lischinski. Blended latent diffusion. *ACM transactions on graphics (TOG)*, 42(4):1–11, 2023.
- [29] Tianqi Chen, Bing Xu, Chiyuan Zhang, and Carlos Guestrin. Training deep nets with sublinear memory cost. *arXiv preprint arXiv:1604.06174*, 2016.
- [30] Paras Jain, Ajay Jain, Aniruddha Nrusimha, Amir Gholami, Pieter Abbeel, Joseph Gonzalez, Kurt Keutzer, and Ion Stoica. Checkmate: Breaking the memory wall with optimal tensor rematerialization. *Proceedings of Machine Learning and Systems*, 2:497–511, 2020.
- [31] Wenhan Xia, Hongxu Yin, Xiaoliang Dai, and Niraj K Jha. Fully dynamic inference with deep neural networks. *IEEE Transactions on Emerging Topics in Computing*, 10(2):962–972, 2021.
- [32] Geng Yuan, Xiaolong Ma, Wei Niu, Zhengang Li, Zhenglun Kong, Ning Liu, Yifan Gong, Zheng Zhan, Chaoyang He, Qing Jin, et al. Mest: Accurate and fast memory-economic sparse training framework on the edge. *Advances in Neural Information Processing Systems*, 34:20838–20850, 2021.
- [33] Jiaze E, Srutarshi Banerjee, Tekin Bicer, Guannan Wang, Yanfu Zhang, and Bin Ren. Fcdm: A physics-guided bidirectional frequency aware convolution and diffusion-based model for sinogram inpainting, 2025.
- [34] Jiaming Song, Chenlin Meng, and Stefano Ermon. Denoising diffusion implicit models. *arXiv preprint arXiv:2010.02502*, 2020.
- [35] Kaiming He, Xinlei Chen, Saining Xie, Yanghao Li, Piotr Dollár, and Ross Girshick. Masked autoencoders are scalable vision learners. In *Proceedings of the IEEE/CVF conference on computer vision and pattern recognition*, pages 16000–16009, 2022.
- [36] Francesco De Carlo, Doğa Gürsoy, Daniel J Ching, K Joost Batenburg, Wolfgang Ludwig, Lucia Mancini, Federica Marone, Rajmund Mokso, Daniël M Pelt, Jan Sijbers, et al. Tomobank: a tomographic data repository for computational x-ray science. *Measurement Science and Technology*, 29(3):034004, 2018.
- [37] K Aditya Mohan, SV Venkatakrishnan, John W Gibbs, Emine Begum Gulsoy, Xianghui Xiao, Marc De Graef, Peter W Voorhees, and Charles A Bouman. Timbir: A method for time-space reconstruction from interlaced views. *IEEE Transactions on Computational Imaging*, 1(2):96–111, 2015.
- [38] Daniel Maria Pelt and Kees Joost Batenburg. Fast tomographic reconstruction from limited data using artificial neural networks. *IEEE Transactions on Image Processing*, 22(12):5238–5251, 2013.

- [39] Stefan Van der Walt, Johannes L Schönberger, Juan Nunez-Iglesias, François Boulogne, Joshua D Warner, Neil Yager, Emmanuelle Gouillart, and Tony Yu. scikit-image: image processing in python. *PeerJ*, 2:e453, 2014.
- [40] Doga Gürsoy, Francesco De Carlo, Xianghui Xiao, and Chris Jacobsen. Tomopy: a framework for the analysis of synchrotron tomographic data. *Journal of synchrotron radiation*, 21(5):1188–1193, 2014.
- [41] Zhou Wang, Alan C Bovik, Hamid R Sheikh, and Eero P Simoncelli. Image quality assessment: from error visibility to structural similarity. *IEEE transactions on image processing*, 13(4):600–612, 2004.
- [42] Robin Rombach, Andreas Blattmann, Dominik Lorenz, Patrick Esser, and Björn Ommer. High-resolution image synthesis with latent diffusion models. In *Proceedings of the IEEE/CVF conference on computer vision and pattern recognition*, pages 10684–10695, 2022.
- [43] F Marone and M Stampanoni. Regridding reconstruction algorithm for real-time tomographic imaging. *Synchrotron Radiation*, 19(6):1029–1037, 2012.

## A Generalization to Other Diffusion-based Inpainting Models

Unless stressed, all experimental settings in Appendix—including hardware, inference configurations, PyTorch optimizations, sampling steps, evaluation metrics—and training strategies are kept identical to those used in the main paper to ensure fair and consistent comparison. To avoid redundancy, many ablation and efficiency-related experiments in the Appendix are presented using a single representative dataset (typically Shape), a fixed resolution ( $1024 \times 1024$ , and a 0.8 mask ratio. This choice reflects the mid-range case in terms of structural complexity and computational load.

### A.1 HiSin as a Model-Agnostic Inference Framework

HiSin is introduced as a unified inference optimization framework, not as an auxiliary enhancement to any specific backbone architecture such as FCDM [33]. Its design is centered around a concrete system-level objective: enabling efficient high-resolution sinogram inpainting under the constraints of GPU memory overhead. To this end, HiSin incorporates three cooperating mechanisms—resolution-guided progressive inference, frequency-aware patch skipping, and structure-adaptive step allocation—that together form a structured inference pipeline. Importantly, these mechanisms do not rely on the internal architecture, loss formulation, or training-time access patterns of any specific model. The framework is architecture-agnostic and training-independent, making it broadly applicable to diffusion models that operate on sinogram inpainting.

The resolution-guided inference module reduces peak memory usage by first processing a downsampled version of the input to extract global features and then using it to gradually refine the input at higher resolutions, a strategy applicable to any model that supports multi-scale inference. The frequency-aware patch skipping mechanism filters out spectrally sparse regions based on FFT-based patch complexity, a general property of sinogram data rather than a model-specific signal. Finally, the structure-adaptive step allocation adjusts denoising iterations per patch based on entropy-derived complexity scores, requiring only access without model-specific conditioning or training-derived priors. None of these designs requires changes to the model’s architecture or parameters.

Taken together, these characteristics ensure that HiSin functions as a standalone inference framework that can be attached to a range of diffusion-based sinogram completion models. While our experiments are built upon FCDM for demonstration, the principles underlying HiSin are compatible with other architectures, such as latent diffusion models and other diffusion-based inpainting methods that follow the DDIM sampling paradigm. This generality allows HiSin to serve as a practical, plug-in optimization system, especially under high-resolution and limited-memory scenarios.

### A.2 Evaluation Results for Other Diffusion Inpainting Models

To further demonstrate that HiSin generalizes beyond FCDM, we apply it to two other diffusion-based inpainting models: CoPaint [18] and Latent Diffusion Model (LDM) [42].

Table 4: Peak GPU memory usage (GB) and inference time (s) for CoPaint and LDM w/ (+) and w/o (-) optimizations from HiSin on different datasets and resolutions. ‘OOM’ indicates out-of-memory failure.

| Method   | Dataset    | 2048×2048 |      | 1024×1024 |      |
|----------|------------|-----------|------|-----------|------|
|          |            | Peak GPU  | Time | Peak GPU  | Time |
| Copaint  | Real-world |           |      | 16.2      | 1.21 |
|          | Shape      | OOM       |      | 16.2      | 1.21 |
|          | Shepp2d    |           |      | 16.2      | 1.21 |
| Copaint+ | Real-world | 26.9      | 2.89 | 11        | 1.01 |
|          | Shape      | 26.9      | 2.89 | 10.9      | 1.01 |
|          | Shepp2d    | 26.9      | 2.89 | 10.9      | 1.01 |
| LDM      | Real-world |           |      | 16.2      | 1.21 |
|          | Shape      | OOM       |      | 16.2      | 1.21 |
|          | Shepp2d    |           |      | 16.2      | 1.21 |
| LDM+     | Real-world | 25.6      | 2.61 | 10.7      | 0.94 |
|          | Shape      | 25.6      | 2.61 | 10.7      | 0.93 |
|          | Shepp2d    | 25.6      | 2.6  | 10.6      | 0.94 |

We begin with evaluating the memory efficiency and inference time. We fix the mask ratio at 0.8 across all models and datasets. This is because memory usage and runtime are primarily determined by resolution and model size, rather than the sparsity pattern of the input mask. As shown in Table 4, the peak memory usage is reduced by up to 29.68% and the runtime is reduced by up to 15.79%.

Table 5: Quantitative SSIM & PSNR comparisons for CoPaint and LDM w/ (+) and w/o (-) optimizations from HiSin across all datasets, resolutions, with a 0.8 mask ratio. For each method, SSIM is shown on the first line, PSNR on the second. Each entry is formatted as: inpainted sinogram (reconstructed CT image by Gridrec [43]), with metrics computed only within masked regions.

|           | Method   | Dataset                      |                              |                              |
|-----------|----------|------------------------------|------------------------------|------------------------------|
|           |          | Real-world                   | Shape                        | Shepp2d                      |
| 2048×2048 | CoPaint  | OOM<br>OOM                   | OOM<br>OOM                   | OOM<br>OOM                   |
|           | CoPaint+ | 0.905 (0.891)<br>28.6 (27.7) | 0.914 (0.902)<br>29.7 (28.8) | 0.925 (0.911)<br>30.4 (29.4) |
|           | LDM      | OOM<br>OOM                   | OOM<br>OOM                   | OOM<br>OOM                   |
|           | LDM+     | 0.888 (0.869)<br>27.7 (26.5) | 0.891 (0.872)<br>28.4 (27.2) | 0.901 (0.884)<br>29.6 (28.4) |
|           | CoPaint  | 0.909 (0.896)<br>28.9 (28.0) | 0.916 (0.904)<br>30.0 (29.3) | 0.928 (0.916)<br>30.9 (30.0) |
| 1024×1024 | CoPaint+ | 0.907(0.897)<br>28.7 (27.3)  | 0.914 (0.902)<br>29.8 (29.0) | 0.926 (0.913)<br>30.6 (29.7) |
|           | LDM      | 0.886 (0.870)<br>27.9 (26.6) | 0.892 (0.875)<br>28.5 (27.3) | 0.906 (0.889)<br>29.9 (28.6) |
|           | LDM+     | 0.883 (0.868)<br>27.8 (26.4) | 0.891 (0.873)<br>28.4 (27.2) | 0.904 (0.886)<br>29.7 (28.5) |
|           | CoPaint  | 0.909 (0.896)<br>28.9 (28.0) | 0.916 (0.904)<br>30.0 (29.3) | 0.928 (0.916)<br>30.9 (30.0) |

For quantitative evaluations, we then calculate the SSIM & PSNR at two resolutions (1024 and 2048) with a 0.8 mask ratio on all three datasets in Table 5. In each case, we report results for both the original version of each model and the version integrated with optimizations from HiSin.

These findings further support our claim that the system-level mechanisms introduced in HiSin are not only effective on FCDM, but also generalize reliably to other diffusion-based sinogram inpainting models without architectural modification or retraining.

## B Applicability to Batched Inference

### B.1 Design Compatibility with Batched Inference

HiSin is designed primarily for memory-constrained high-resolution inference, where batch size is often set to 1 due to practical hardware limitations in clinical or industrial CT pipelines. Nevertheless, the framework itself does not assume or rely on singleton inference in any way.

All three optimization mechanisms in HiSin—resolution-guided progressive inference, frequency-aware patch skipping, and structure-adaptive step allocation—operate at the per-sample or per-patch level. They do not involve any batch-dependent computation, nor do they rely on inter-sample interactions. As a result, HiSin remains fully compatible with batched inference settings as long as sufficient GPU memory is available.

### B.2 Batched Inference Results

We evaluate both the baseline model FCDM and HiSin at batch size of 2. Since dataset, mask ratio, and resolution are not highly related to batch size, we only show the results on Shape with a 0.8 mask ratio and a fixed resolution 1024 × 1024. As shown in Table 6, both peak GPU memory and inference time are reduced with only negligible variation on SSIM and PSNR.

These results reinforce the claim that HiSin is a batch-agnostic inference framework. It can be safely deployed in both singleton and batched inference scenarios without modification.

Table 6: Inference performance of FCDM and HiSin when batch size is 2. Experiments are conducted on Shape at  $1024 \times 1024$  resolution with a 0.8 mask ratio. SSIM and PSNR are formatted as: inpainted sinogram (reconstructed CT image by Gridrec), with metrics computed only within masked regions.

| Method | Peak GPU (GB) | Time (s) | SSIM          | PSNR        |
|--------|---------------|----------|---------------|-------------|
| FCDM   | 28.3          | 1.20     | 0.939 (0.925) | 31.4 (30.5) |
| HiSin  | 15.9          | 0.77     | 0.937 (0.924) | 31.3 (30.4) |

## C Additional Design Notes about Hyperparameter Choices

### C.1 Sensitivity of the Patch-Skipping Threshold

#### C.1.1 Rationale Behind the Patch-Skipping Threshold Selection

The parameter  $\tau$  controls the patch-skipping threshold in HiSin. Specifically, it determines the spectral energy level below which a patch is considered uninformative and thus can be skipped during inference. A larger value of  $\tau$  results in more aggressive skipping, while a smaller value leads to fewer patches being skipped and then higher inference time.

We set  $\tau = 0.08$  in all our experiments based on three practical considerations:

- Empirical coverage of low-frequency components: In typical sinogram inputs, a threshold of 0.08 allows us to skip patches with minimal high-frequency activity while still retaining structurally important information.
- Interpretability and reproducibility: Compared to more aggressive thresholds, the 0.08 setting avoids dropping structurally ambiguous or borderline patches.
- Stability across datasets and resolutions: We observed that  $\tau = 0.08$  yields stable performance across all datasets, and across multiple input resolutions and mask ratios. This suggests that the choice is not overly sensitive to dataset-, input resolution- or mask ratio-specific properties.

These empirical observations collectively support the choice of  $\tau = 0.08$  as a robust and balanced default.

#### C.1.2 Sensitivity Analysis Experiments

Table 7: Sensitivity of HiSin to different values of  $\tau$  on Shape with a  $1024 \times 1024$  resolution and a 0.8 mask ratio. SSIM and PSNR are formatted as: inpainted sinogram (reconstructed CT image by Gridrec), with metrics computed only within masked regions.

| $\tau$ | SSIM          | PSNR        |
|--------|---------------|-------------|
| 0.12   | 0.930 (0.918) | 30.8 (29.6) |
| 0.08   | 0.937 (0.925) | 31.5 (30.6) |
| 0.05   | 0.938 (0.927) | 31.6 (30.6) |

Table 7 reports evaluation results for  $\tau$  sensitivity on Shape at  $1024 \times 1024$  resolution, with a fixed mask ratio of 0.8. We compare SSIM and PSNR under three representative values of  $\tau$ : 0.12, 0.08, and 0.05. These thresholds respectively correspond to aggressive skipping, default setting, and conservative skipping.

we observed that decreasing  $\tau$  beyond 0.08 yields diminishing returns in inpainting accuracy, while causing an increase in inference time due to the larger number of patches retained. Therefore, we set  $\tau = 0.08$  as a practical balance point—preserving computational efficiency without sacrificing output quality.

### C.2 Choices of Other Hyperparameters

**Resolution fusion weights  $\lambda_{mid}$  and  $\lambda_{high}$ .** Both  $\lambda_{mid}$  and  $\lambda_{high}$  are set to 0.5, balancing the influence of lower-resolution priors including global features with high-resolution structural details during progressive inference.

**Gradient threshold  $\eta$  for patch blending.** We set  $\eta = 0.1$  to balance efficiency and visual quality in patch stitching. A lower threshold would lead to unnecessary computation with negligible benefit. A higher threshold risks skipping blending in structurally significant areas, causing visible seams.

**Sigmoid sharpness factor  $\beta$ .** We set the sigmoid sharpness factor  $\beta = 5$  to achieve a smooth but sufficiently discriminative mapping from complexity scores to denoising step counts.

### C.3 Distinction Between Patch Skipping and Adaptive Step Allocation

While both patch skipping and adaptive step allocation rely on local complexity analysis, they serve distinct purposes and operate under different assumptions. Patch skipping is a coarse-grained gating mechanism that identifies structurally trivial regions where full denoising can be omitted entirely. It uses a simple frequency-domain criterion—the ratio of high-frequency energy—to detect spectrally sparse patches dominated by very smooth or empty content. This decision is binary and conservative: a skipped patch will never undergo any denoising, so the threshold must be set cautiously to avoid quality degradation.

In contrast, adaptive step allocation aims to adjust the computational effort spent on patches that are retained for inference. Instead of deciding whether to process a patch, it modulates how many DDIM steps to apply based on a richer complexity score. This score combines Shannon entropy over pixel intensities with the total frequency energy (via the L1 norm of the FFT), capturing both spatial irregularity and spectral richness. The resulting step count is assigned through a smooth sigmoid mapping centered around the mean complexity across all patches, ensuring stable and data-aware inference depth scheduling.

While both mechanisms involve complexity estimation, their criteria, granularity, and functional roles are fundamentally different.

## D Per-Dataset Evaluation Details

Table 8: Peak GPU memory usage (GB) and inference time (s) for HiSin and FCDM on different datasets and resolutions. 'OOM' indicates out-of-memory failure.

| Method       | Dataset    | 2048×2048 |      | 1024×1024 |      | 512×512  |      |
|--------------|------------|-----------|------|-----------|------|----------|------|
|              |            | Peak GPU  | Time | Peak GPU  | Time | Peak GPU | Time |
| HiSin (ours) | Real-world | 24.9      | 2.22 | 8.7       | 0.78 | 3.3      | 0.4  |
|              | Shape      | 24.9      | 2.21 | 8.7       | 0.78 | 3.2      | 0.4  |
|              | Shepp2d    | 24.8      | 2.21 | 8.7       | 0.76 | 3.3      | 0.3  |
| FCDM         | Real-world |           |      | 16.2      | 1.21 | 5.3      | 0.6  |
|              | Shape      | OOM       |      | 16.2      | 1.22 | 5.2      | 0.6  |
|              | Shepp2d    |           |      | 16.1      | 1.21 | 5.2      | 0.5  |

To assess the generality of our optimizations, we provide detailed results across three datasets: *Real-world*, *Shape*, and *Shepp2d*. As shown in Table 8 and Table 9, the peak memory usage and inference time remain stable across datasets and the differences in SSIM and PSNR between HiSin and FCDM are consistently small. These results suggest that our optimization strategies are robust and dataset-independent.

## E Limitations: Computational Cost Analysis

While HiSin improves memory usage and inference speed through hierarchical scheduling and patch-level optimization, it comes with a moderate increase in total FLOPs compared to other efficiency-oriented baselines. As shown in Table 10, HiSin incurs an average of 25.9% more FLOPs than DiffIR. This reflects the structural overhead of progressive inference and adaptive patch processing. While the FLOPs slightly increase compared to DiffIR, this trade-off is necessary to support higher resolution sinogram inpainting, while maintaining high memory efficiency and inpainting quality.

Table 9: Quantitative SSIM & PSNR comparisons across all datasets, resolutions, and mask ratios. For each method, SSIM is shown on the first line, PSNR on the second. SSIM and PSNR are formatted as: inpainted sinogram (reconstructed CT image by Gridrec), with metrics computed only within masked regions.

|           | Methods      | Dataset    | Mask ratio    |               |               |
|-----------|--------------|------------|---------------|---------------|---------------|
|           |              |            | 0.4           | 0.6           | 0.8           |
| 2048×2048 | HiSin (ours) | Real-world | 0.911 (0.899) | 0.920 (0.907) | 0.924 (0.911) |
|           |              |            | 29.5 (28.7)   | 29.9 (29.1)   | 29.8 (28.9)   |
|           |              | Shape      | 0.922 (0.910) | 0.930 (0.918) | 0.933 (0.921) |
|           |              |            | 30.6 (29.5)   | 30.8 (29.4)   | 30.9 (29.9)   |
|           |              | Shepp2d    | 0.931 (0.919) | 0.940 (0.927) | 0.944 (0.931) |
|           |              |            | 31.6 (30.8)   | 32.0 (31.3)   | 31.8 (30.7)   |
|           | FCDM         | Real-world |               |               |               |
|           |              | Shape      |               | OOM           |               |
|           |              | Shepp2d    |               |               |               |
|           |              |            |               |               |               |
| 1024×1024 | HiSin (ours) | Real-world | 0.917 (0.904) | 0.924 (0.912) | 0.928 (0.915) |
|           |              |            | 30.3 (29.5)   | 30.4 (29.6)   | 30.4 (29.5)   |
|           |              | Shape      | 0.927 (0.913) | 0.935 (0.921) | 0.937 (0.923) |
|           |              |            | 30.4 (29.7)   | 30.4 (29.7)   | 30.4 (29.6)   |
|           |              | Shepp2d    | 0.937 (0.925) | 0.944 (0.933) | 0.948 (0.936) |
|           |              |            | 31.3 (30.6)   | 31.5 (30.8)   | 31.5 (30.9)   |
|           | FCDM         | Real-world | 0.918 (0.906) | 0.925 (0.912) | 0.928 (0.916) |
|           |              |            | 30.4 (29.7)   | 30.4 (29.7)   | 30.4 (29.6)   |
|           |              | Shape      | 0.928 (0.914) | 0.935 (0.921) | 0.938 (0.924) |
|           |              |            | 31.3 (30.6)   | 31.6 (30.9)   | 31.5 (30.9)   |
|           |              | Shepp2d    | 0.938 (0.926) | 0.944 (0.932) | 0.948 (0.936) |
|           |              |            | 32.4 (31.6)   | 32.6 (31.8)   | 32.6 (31.8)   |
| 512×512   | HiSin (ours) | Real-world | 0.913 (0.901) | 0.919 (0.906) | 0.924 (0.911) |
|           |              |            | 0.1 (29.4)    | 30.3 (29.6)   | 30.5 (29.7)   |
|           |              | Shape      | 0.923 (0.910) | 0.933 (0.918) | 0.933 (0.919) |
|           |              |            | 31.2 (30.5)   | 31.5 (30.6)   | 31.5 (30.7)   |
|           |              | Shepp2d    | 0.933 (0.921) | 0.939 (0.926) | 0.944 (0.933) |
|           |              |            | 32.3 (31.6)   | 32.5 (31.8)   | 32.7 (31.9)   |
|           | FCDM         | Real-world | 0.913 (0.902) | 0.919 (0.907) | 0.924 (0.912) |
|           |              |            | 30.2 (29.7)   | 30.3 (29.7)   | 30.5 (29.8)   |
|           |              | Shape      | 0.924 (0.911) | 0.933 (0.919) | 0.934 (0.920) |
|           |              |            | 31.2 (30.5)   | 31.5 (30.6)   | 31.5 (30.7)   |
|           |              | Shepp2d    | 0.934 (0.922) | 0.939 (0.926) | 0.944 (0.933) |
|           |              |            | 32.4 (31.7)   | 32.5 (31.8)   | 32.7 (31.9)   |

Table 10: FLOPs (G) for different methods varied input resolutions on Real-world with a 0.8 mask ratio. 'OOM' indicates out-of-memory failure. All FLOPs are estimated via code-level calculation based on resolution, patch size, and denoising steps. These calculations are performed using standard layer-wise formulas, without reliance on hardware profiling.

| Method       | 2048×2048 | 1024×1024 | 512×512 |
|--------------|-----------|-----------|---------|
| FCDM         | OOM       | 7.81      | 2.04    |
| DiffIR       |           | 4.52      | 1.12    |
| HiDiffusion  | 20.6      | 5.42      | 1.34    |
| HiSin (ours) | 21.5      | 5.65      | 1.42    |